Microbubble shape oscillations excited through ultrasonic parametric driving

Michel Versluis,[1] David E. Goertz,[2] Peggy Palanchon,[2] Ivo L. Heitman,[1] Sander M. van der Meer,[1] Benjamin Dollet,[1] Nico de Jong,[1,2] and Detlef Lohse[1,*]

[1]*Physics of Fluids Group, Department of Science and Technology, J.M. Burgers Research Center for Fluid Mechanics, IMPACT, MESA+, and MIRA Research Institutes, University of Twente, P.O. Box 217, 7500 AE Enschede, The Netherlands*

[2]*Department of Experimental Echocardiography, Erasmus MC, P.O. Box 1738, 3000 DR Rotterdam, The Netherlands*

(Received 12 September 2007; revised manuscript received 21 June 2010; published 30 August 2010)

An air bubble driven by ultrasound can become shape-unstable through a parametric instability. We report time-resolved optical observations of shape oscillations (mode $n=2$ to 6) of micron-sized single air bubbles. The observed mode number n was found to be linearly related to the ambient radius of the bubble. Above the critical driving pressure threshold for shape oscillations, which is minimal at the resonance of the volumetric radial mode, the observed mode number n is independent of the forcing pressure amplitude. The microbubble shape oscillations were also analyzed numerically by introducing a small nonspherical linear perturbation to a Rayleigh-Plesset-type equation, capturing the experimental observations in detail.

DOI: 10.1103/PhysRevE.82.026321 PACS number(s): 47.55.dd, 43.25.+y

I. INTRODUCTION

Bubbles insonified by ultrasound will generally exhibit a radial oscillation mode. In addition, surface modes can be generated, which have been studied extensively for millimeter-sized bubbles [1,2] and droplets [3–6]. Surface mode vibrations for bubbles were analyzed theoretically by Plesset [7], Strasberg [8], Neppiras [9], Eller [10], Prosperetti [11], and Benjamin [12,13] (see also his earlier papers cited in these references). In recent years the coupling between translation bubble motion and acoustically triggered bubble shape oscillations has been addressed in [14,15]. The overwhelming interest in sonoluminescing bubbles in the nineties led to investigations into surface mode oscillations for micron-sized and millimeter-sized bubbles by several groups [1,16–25]. Under sonoluminescing conditions the microbubbles are driven far away from their volumetric resonance frequency at relatively high acoustic pressures up to 150 kPa. The fast time scales under which transients of shape oscillations occur have hitherto limited the observations to either photographic snapshots [25] or to a stroboscopic multipulsing approach (see, e.g., [26]). Mie scattering, see also [26], only allows to judge that bubble undergo shape oscillations, but no shape mode can be identified.

Here we overcome the difficulties of the direct observations of the surface modes through the use of ultrafast imaging. We conducted a set of controlled experiments for a variety of bubble radii, while investigating the onset of microbubble shape vibrations, fully resolved in time through the use of ultrahigh-speed imaging at 1 million frames per second. The bubbles were driven near their volumetric resonance frequency at mild acoustic pressures as to allow the surface modes to build up during insonation through a parametric instability.

Finally, we note that deducing results from millimeter-sized bubbles to micrometer-sized bubbles is nontrivial, as for the latter bubbles viscous effects become important. Those are quantified by the Ohnesorge number, which compares viscous and capillary forces. For the nth order shape mode the relevant length scale is $\ell_n = R_0/2n$ [19], where R_0 is the ambient bubble radius. The Ohnesorge number for the dynamics of mode-n oscillations of a bubble is thus

$$\mathrm{Oh}_n := \sqrt{\frac{\nu^2\rho}{\ell_n\sigma}} = \sqrt{\frac{2n\nu^2\rho}{R_0\sigma}}. \tag{1}$$

Putting the typical values for the water kinematic viscosity ν, its surface tension σ, and its density ρ, one obtains for a $R_0 = 10$ μm bubble $\mathrm{Oh}_n \approx 0.053\sqrt{n}$, which reveals that (i) viscous effects become of increasing importance for higher surface modes and (ii) that they can no longer be neglected for micron-sized bubbles.

II. EXPERIMENTS

Single air bubbles with a radius ranging from 10 to 45 μm were generated in a regulated coflow micropipette injector described in [27]. The injector allowed for a controlled production of microbubbles, both in radius and in separation distance. The bubbles were left to rise in purified water to the test section at a downstream distance from the injector. The bubbles were insonified with an ultrasound pulse from an unfocused single element piezoelectric transducer consisting of a burst of 10 cycles at a frequency of 130 kHz. The bubble dynamics was recorded with the Brandaris high-speed camera described in [29]. The rotating mirror of the camera sweeps the incoming image along a quarter arc containing 128 highly sensitive charge-coupled devices. With a mirror rotation speed of 20 000 rps a frame rate of 25 million frames per second can be achieved. The camera data controller system allows for six consecutive recordings of 128 frames each. This functionality was used to insonify the very same bubble at increasing acoustic pressures in six incremental steps from 0 to 50 kPa for the smaller microbubbles ($R_0 < 25$ μm) and from 0 to 150 kPa for the larger ones.

Figure 1(a) shows a selection of a high-speed recording displaying the dynamics of a 36 μm radius bubble driven at

*d.lohse@utwente.nl

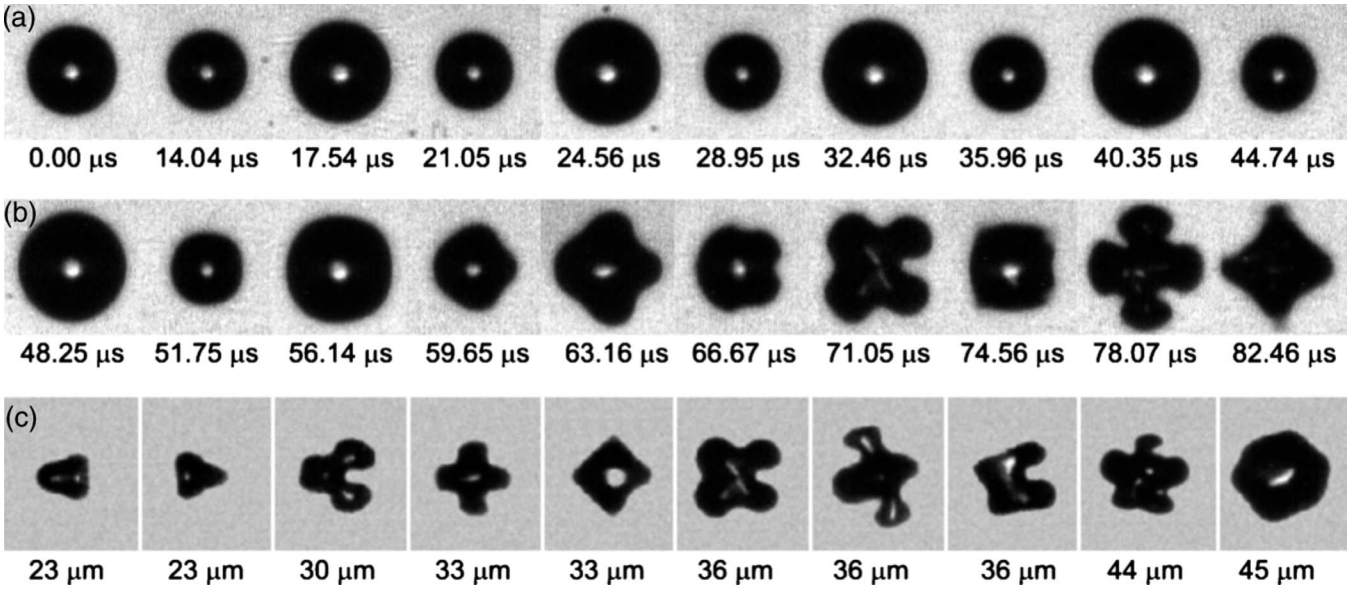

FIG. 1. Growth of a surface mode vibration for a bubble with a radius of 36 μm as captured with the Brandaris high-speed camera. First, the bubble oscillates in a purely volumetric radial mode (a), then after 5 cycles of ultrasound (b) the bubble becomes shape-unstable and a surface mode $n=4$ is formed [28]. (c) A selection of surface modes observed for various bubble radii.

an acoustic pressure of 120 kPa. The first frame shows the bubble at rest; the next nine frames show how the bubble oscillates radially in a spherical volumetric mode. Figure 1(b) shows the situation after 5 cycles of ultrasound (40 μs after ultrasound arrival) where the bubble develops a surface mode vibration, here with a mode number $n = 4$. Soon after the acoustic driving stops, the surface mode vibration decays quickly and the bubble recovers its spherical shape. Many types of surface wave vibration were observed in the course of the experiments and a compilation of these is given in Fig. 1(c).

The experimental analysis is illustrated in Fig. 2. Here a bubble with an ambient radius of $R_0=33$ μm is insonified with a driving pulse with a pressure of 120 kPa at a frequency $f=130$ kHz [Fig. 2(a)], and recorded at a frame rate of 1.13 Mfps. The high-speed recordings were processed through a dynamic programming contour tracing algorithm described in [30] resulting in the ambient radius of the bubble R_0 and the position of the center of mass of the bubble as a function of time. From the center of mass the angular dependence of the radius $R(\theta,t)$ of the bubble was measured as a function of the angle θ [Fig. 2(b)] and time t, see Fig. 2(c) for the plot at $t=80$ μs. The radial oscillations of the bubble $R(t)$ were extracted from the mean of $R(\theta,t)$ and are plotted in Fig. 2(d). A Fourier analysis of the bubble surface distortions resulted in a spectrum from which the amplitude of the surface wave mode numbers was determined, see Fig. 2(e). Figure 2(f) shows the time evolution of the most instable mode of order 4. Figure 2(g) displays the same curve in a log-linear scale.

From the analysis of the full set of experiments it followed, first, that all bubbles initially oscillate in a purely spherical mode. Second, we noticed that, beyond a critical threshold of the acoustic pressure, surface modes can be generated after several acoustic cycles. The threshold depends on the ambient bubble radius and is minimal for bubbles

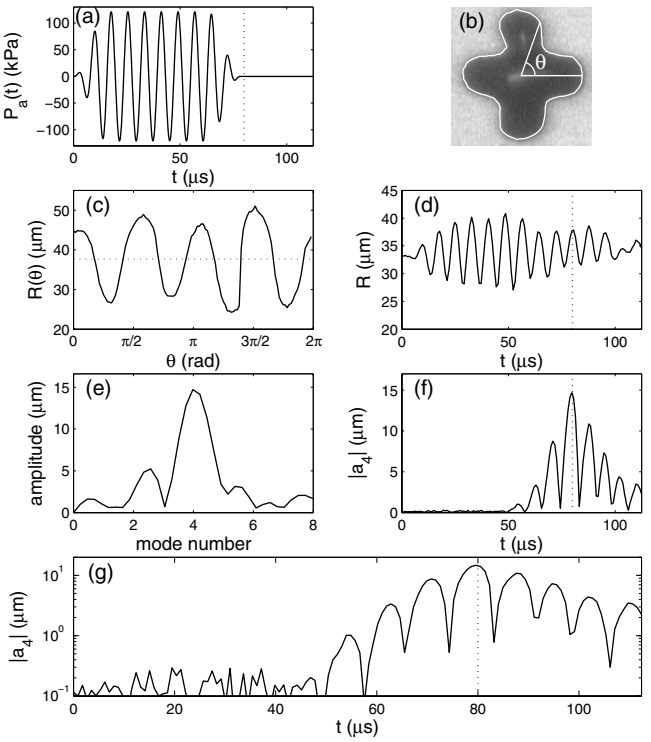

FIG. 2. Experimental analysis. In (a) the driving pressure pulse $P_a(t)$ is shown, which drives a bubble with an ambient radius of 33 μm. (b) shows an image of the shape-unstable bubble at $t=80$ μs. In (c) the radial excursion is plotted against the polar angle θ, at $t=80$ μs. (d) shows the volumetric response of the bubble. (e) displays the amplitude of mode number n which is derived from the Fourier transform of (c), and the time evolution of the growth of the shape instability of order 4 is shown in (f) and (g), in a linear-linear and a log-linear scale, respectively. The dotted lines in (a), (d), (f), and (g) indicate $t=80$ μs.

close to the volumetric resonance size of 25 μm at 130 kHz driving. Third, it was observed that bubbles have a preferential surface wave mode number which increases linearly with increasing bubble size. Finally, we found that the preferential surface wave mode number does not depend on the forcing pressure of the ultrasound burst, provided of course it is beyond the threshold.

For the mildly oscillating bubbles studied here the most relevant surface instability is that of the parametric instability [19,24]. It exhibits maximal growth when the time scale of the acoustic forcing is of the order of the time scale of the natural volumetric oscillation frequency. Figure 2(g) indicates that the surface mode amplitude grows exponentially from cycle-to-cycle and therefore the bubble shape oscillations must be induced by such a parametric instability, acting on an initial distortion of submicron scale.

One wonders on whether the initial distortion and thus also the final orientations of the surface modes follow a preferred direction. There are three preferred directions in the system: (i) gravity, (ii) the orientation of the ultrasound beam which was perpendicular to gravity, and (iii) the direction of the neighboring bubbles which was the same as gravity. From the high-speed movies we find that the axis of symmetry of the surface modes is always in the horizontal direction. Both gravity and neighboring bubbles would result in surface mode oscillations with an axis of symmetry in the vertical direction. Note that the preferred orientation can only be inferred from the odd mode numbers, see, e.g., the smallest bubbles with a mode 3 in Fig. 1(c). For even mode numbers we cannot indicate the axis of symmetry being vertical or horizontal because of (another) symmetry of the surface modes.

As a generic feature of a parametric instability [31], the most unstable case, or parametric resonance, arises for $\omega = 2\omega_n$, where $\omega = 2\pi f$ and where the natural frequency of oscillation ω_n of a given surface mode n is given by [32]

$$\omega_n^2 = (n-1)(n+1)(n+2)\frac{\sigma}{\rho R_0^3}, \tag{2}$$

with σ the surface tension and ρ the density of the liquid. For a fixed driving frequency Eq. (2) indicates, in first order, a linear relationship between the mode number n and R_0, as observed in experiment. We plot the observed preferential surface mode numbers n as a function of R_0 in the bottom part of Fig. 3. The gray dots represent Eq. (2) and it is seen that the experimental data conform to the classical Lamb expression very well. How the modes compete over the full range of bubble radii requires a more detailed numerical analysis as will be discussed in the next section.

Equation (2) together with figures of the type 2(g) also allow to double-check the value of the surface tension: e.g., the Fourier transformation of the decaying part of curve in Fig. 2(g) (i.e., beyond the dotted vertical line where the driving has stopped) for the $R_0 = 33$ μm bubble gives the eigenfrequency $\omega_4 = 65.3$ kHz, from which we deduce $\sigma = 0.067$ N/m. This value is only slightly smaller than that for pure water ($\sigma = 0.072$ N/m), suggesting at most moderate interface contaminations by surfactants.

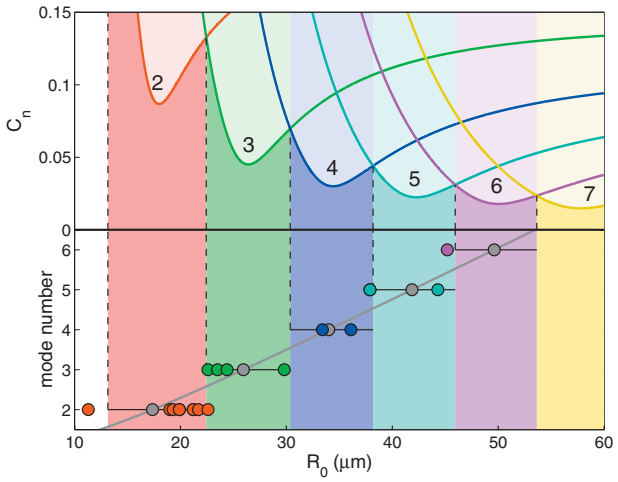

FIG. 3. (Color) Bottom part. Colored dots: the observed mode number n as a function of the ambient bubble radius R_0 for the driving frequency of $f = 130$ kHz. Grey dots: the resonant mode number n following Lamb's expression [Eq. (2)]. Upper part: Solid lines represent the pulsation amplitude threshold C_n following Ref. [33]. The lowest threshold preferentially selects the mode number n indicated by the colored bars.

Figure 4 displays all of our experimental data points on surface mode vibrations in the ambient bubble radius R_0 vs forcing pressure P_a phase space. White circles correspond to shape-stable bubbles and colored ones to some observed respective shape mode. Bubbles around the resonance radius of 25 μm are most vulnerable toward shape instabilities.

A similar phase diagram for the shape instabilities for a driving with a much lower frequency $f = 20$ kHz was measured by Gaitan and Holt [25], see Fig. 3 of that paper. For that case the resonance radius is around 160 μm, where the shape modes were not probed in Ref. [25], so that the reso-

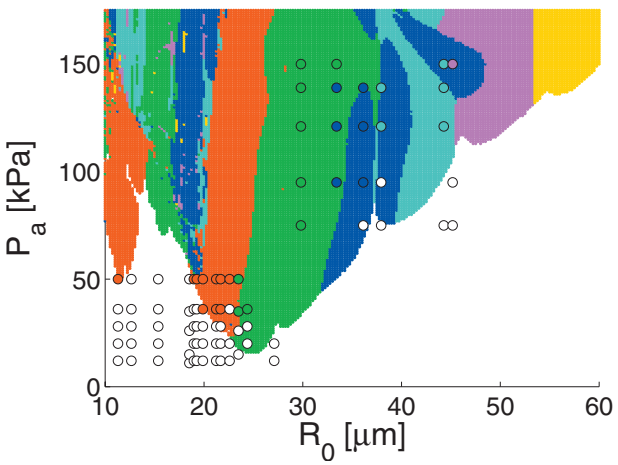

FIG. 4. (Color) Phase diagram in R_0 vs P_a space for the driving frequency of $f = 130$ kHz. Every experimental data point is included as a circle: white—no shape mode detected, red—mode 2, green—mode 3, blue—mode 4, turquoise—mode 5, magenta—mode 6, and yellow—mode 7. For comparison, also the theoretical result is shown. The color coding indicates the specific mode preference and corresponds to the coding used for the experimental data.

nance structure of the onset of shape instabilities could not be seen, since the largest bubbles in Ref. [25] were only around $R_0=100$ μm.

III. THEORETICAL RESULTS

Francescutto and Nabergo [33] analyzed the onset of the parametric instability leading to surface mode vibrations, following the spherical stability analysis of [11], by expressing the amplitude threshold of the radial oscillations required for the instability to develop. The mode dynamics were expressed as a Mathieu equation, based on a linearized Rayleigh-Plesset equation. The analysis was limited to the subresonance oscillations. The separation line between shape-stable and shape-unstable regions then determines the pulsation amplitude threshold C_n for mode n, whose calculation is detailed in [33]. As shown in Fig. 3 the preferred surface mode can be derived from the lowest of each thresholds. These correspond to the bottom part of the figure containing the experimental data points. We find excellent agreement between experiment and theory.

We now look in more detail into the growth mechanism of the surface mode vibration. The parametric instability manifests itself in the growth of initially small perturbations on the spherical interface: $R(\theta,t)=R(t)+a_n(t)Y_n(\theta)$ where $Y_n(\theta)$ is the spherical harmonic of order n and $a_n(t)$ is the amplitude of the surface mode. $R(t)$ is solved from an equation of Rayleigh-Plesset type [34],

$$\left(1-\frac{\dot{R}}{c}\right)R\ddot{R}+\frac{3}{2}\dot{R}^2\left(1-\frac{\dot{R}}{3c}\right)=-\frac{4\nu\dot{R}}{R}-\frac{2\sigma}{\rho R}+\left(1+\frac{\dot{R}}{c}\right)\frac{1}{\rho}[p_g(t)-P_a(t)-P_0]+\frac{R\dot{p}_g(t)}{\rho c}, \tag{3}$$

where $P_a(t)$ represents the forcing pressure, P_0 is the ambient pressure, and c the speed of sound in the liquid. Equation (3) includes the important damping terms, such as radiation damping and viscous damping. While thermal damping is often empirically modeled by an increased viscous damping term in Eq. (3), see, e.g., [35,36], we included thermal damping through the more physical picture recently introduced by [37]. From their extended model we included the bubble hydrodynamics, the gas pressure p_g, and the heat exchange between the gas core and the surrounding liquid. As the bubbles in our study were only weakly driven, we do not include chemical reactions of the gaseous species in the bubble. In addition, for simplicity we chose to model the gas interior to be comprised of nitrogen gas only, which for the present purposes is a good approximation for air. The set of four first order ODE's for R, $\dot{R}$, $\ddot{R}$ and the temperature T was closed by deriving the equation for $\dot{T}(t)$ following [37,38], then solved numerically with a stiff differential solver.

Following the spirit of the classical derivation of the Rayleigh-Plesset equation, a dynamical equation for the distortion amplitude $a_n(t)$ can be derived, see [11,19,24], namely,

$$\ddot{a}_n+B_n(t)\dot{a}_n-A_n(t)a_n=0. \tag{4}$$

As detailed in [19], the amplitudes $A_n(t)$ and $B_n(t)$ can be calculated from the radial dynamics $R(t)$ applying a boundary layer approximation, which at the scale of micrometer-sized bubbles is important to properly account for viscous effects. The result of this calculation is [19]

$$A_n(t)=(n-1)\frac{\ddot{R}}{R}-\frac{\beta_n\sigma}{\rho R^3}+\frac{2\nu\dot{R}}{R^3}\times\left[-\beta_n+n(n-1)(n+2)\frac{1}{1+2\frac{\delta}{R}}\right], \tag{5}$$

$$B_n(t)=\frac{3\dot{R}}{R}+\frac{2\nu}{R^2}\left[-\beta_n+\frac{n(n+2)^2}{1+2\frac{\delta}{R}}\right], \tag{6}$$

with $\beta_n=(n-1)(n+1)(n+2)$ and the thickness of the viscous boundary layer around the bubble approximated as

$$\delta=\min(\sqrt{\nu/\omega},R/2n). \tag{7}$$

We note that by applying Eq. (4) we neglect nonlinear effects and also possible coupling between different modes and to the translational motion of the bubble [13]. These effects can be included in the analysis as, e.g., done in Ref. [14], but the good agreement between experiment and theory demonstrated below shows that the linear analysis is sufficient to describe growth rates even for seemingly large nonspherical distortions as those shown in Fig. 1. Note that for much larger bubbles—order of magnitude 2–3 mm in radius—indications for mode coupling have been found [21].

Equation (4) was solved together with Eq. (3) to give the distortion amplitude $a_n(t)$ for each mode n. A small distortion was imposed to the differential equation of the shape oscillations as an initial condition. The initial distortion decays if the system is driven below threshold. Vice versa, the surface mode will grow rapidly when driven above the threshold of the instability. In the calculations presented here the initial distortion was taken to be 1 nm, in the order of 10^{-4} of the ambient radius of the bubble. We note that the choice of the initial distortion amplitude is arbitrary as we consider a linear perturbation model for the shape instability. Therefore, without any knowledge of the initial condition, the absolute amplitude of the resulting shape deformation cannot be inferred from the model.

The nonspherical oscillation amplitude of a 30 μm radius bubble driven with a burst of 10 cycles of 130 kHz at a pressure of 80 kPa is shown in Figs. 5(a) and 5(b). The graph displays the development over time of the shape oscillations for mode $n=2$ to 7. The mode amplitudes were normalized to the maximum value of all $a_n(t)$. It is seen that the mode $n=3$ grows exponentially while other modes are hardly excited. The finite length of the ultrasound pulse terminates further growth as soon as the parametric driving stops. It is followed by an exponential amplitude decrease with an exponent increasing with the mode number n. The oscillation frequency of the decaying shape modes is characterized by

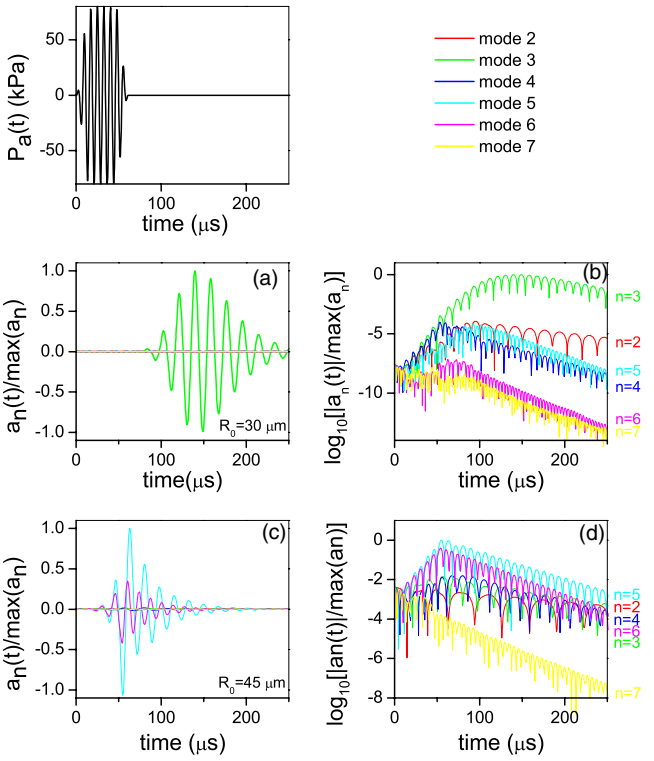

FIG. 5. (Color online) Numerical simulation of the onset of the shape oscillation. (top) An ultrasound pulse of 10 cycles of 130 kHz at a driving pressure of 80 kPa. (a): mode amplitude $a_n(t)$ for $n = 2$ to 7 for a 30 μm radius bubble. The mode $n=3$ appears to be the most unstable mode. (b): the very same result plotted on a log-linear scale showing the exponential growth of the various modes. (c) and (d): similar calculations for a 45 μm bubble, where $n=5$ is the most unstable mode.

its natural frequency [Eq. (2)]. Figures 5(c) and 5(d) show how a dominant mode $n=5$ develops for a bubble of 45 μm radius, while a mode $n=6$ shows an onset of a possible instability, but not nearly as strong as the dominant mode.

To allow for comparison with the experimental phase diagram Fig. 4, the above calculations were repeated for a complete parameter range as a function of the ambient bubble radius R_0 and the forcing pressure P_a. The bubble radius was varied from 10 to 60 μm in 0.25 μm intervals; the pressure was varied from 0 to 175 kPa in 1 kPa incremental steps. The results of these 35 000 calculations were then included into the experimental phase diagram Fig. 4. The numerical data points are classified in color coding following their mode preference, i.e., the mode number with the dominant distortion. In a linear model the choice for the threshold cannot be other than arbitrary. Therefore the experimentally shape-stable bubbles were used to specify the threshold value for surface mode vibrations in the phase diagram. The best fit was obtained when an initial shape distortion was allowed to grow by three orders of magnitude in order to assign the corresponding point (R_0, P_a) in the phase diagram as shape-unstable.

The correspondence between experimental and theoretical results is very good. Just as in experiment, we observe that the forcing pressure threshold for surface mode vibrations has its minimum value at an ambient radius of 25.1 μm, which, as expected, very well coincides with the resonance radius of the natural volumetric oscillation when driven at with a frequency of 130 kHz. The good agreement between experiment and theory also further justifies the boundary layer approximation of [1,19], in addition to the evidence already given by Brenner *et al.* [39], who compared the results of the boundary layer approximations with the experimental results of Ref. [17] and the numerical results of Ref. [22].

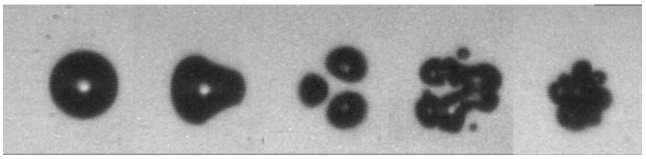

FIG. 6. Splitting of a shape-unstable bubble of surface mode $n=3$: Three fragments are split off.

From the phase diagram in radius vs pressure phase space (Fig. 4) it also follows that the mode preference for a given ambient bubble radius is hardly influenced by the forcing pressure. Furthermore, we notice from the numerical simulations that the instability can grow to a size of the order of the resting radius of the bubble. In experiment such a bubble would split up, as indeed observed in experiment, see Fig. 6. It is interesting to see that the number of initial fragments is directly related to the mode number. For example, Fig. 6 shows a bubble that exhibits a $n=3$ surface mode vibration and then initially splits up into three fragments. The fragmentation then continues toward even smaller bubbles. Theoretically the number of fragments should follow a cubic dependence on the mode number n [40], thus here into 27 fragments. In our setup however, the total number of bubble fragments cannot be tracked quantitatively as there is a fair amount of optical shielding.

IV. CONCLUSIONS AND OUTLOOK

In conclusion, we could monitor the shape instabilities and unstable modes $n=2$ to $n=6$ of microbubbles in the range between 10 and 60 μm, by ultrafast imaging. The comparison with the linear stability analysis, based on an extended Rayleigh-Plesset type approach, gave excellent quantitative agreement. The bubbles close to resonance of the radial oscillations were found to be most vulnerable toward shape instabilities. Above the threshold of shape instability, the observed mode number n is independent of the driving pressure. These results indicate that—at least in the driving pressure regime and for the excitation times analyzed in this paper—surface modes do not couple with each other. We note that recently Dollet *et al.* [41] presented experimental evidence that in contrast microbubbles coated with a polymer or lipid shell (i.e., ultrasound contrast agents) do show such a surface mode coupling. It remains a task for future work to extend our theoretical analysis to such coated bubbles, which are of great importance in medical ultrasound imaging.

[1] C. E. Brennen, *Cavitation and Bubble Dynamics* (Oxford University Press, Oxford, 1995).
[2] T. G. Leighton, *The Acoustic Bubble* (Academic, London, 1994).
[3] P. L. Marston and S. G. Goosby, Phys. Fluids **28**, 1233 (1985).
[4] T. S. Lundgren and N. N. Mansour, J. Fluid Mech. **194**, 479 (1988).
[5] O. A. Basaran, J. Fluid Mech. **241**, 169 (1992).
[6] R. E. Apfel *et al.*, Phys. Rev. Lett. **78**, 1912 (1997).
[7] M. Plesset, J. Appl. Phys. **25**, 96 (1954).
[8] M. Strasberg, J. Acoust. Soc. Am. **28**, 20 (1956).
[9] E. A. Neppiras, J. Acoust. Soc. Am. **46**, 587 (1969).
[10] A. Eller and L. A. Crum, J. Acoust. Soc. Am. **47**, 762 (1970).
[11] A. Prosperetti, Q. Appl. Math. **34**, 339 (1977).
[12] T. B. Benjamin and A. T. Ellis, J. Fluid Mech. **203**, 419 (1989).
[13] T. B. Benjamin and A. T. Ellis, J. Fluid Mech. **212**, 65 (1990).
[14] S. J. Shaw, Phys. Fluids **18**, 072104 (2006).
[15] S. J. Shaw, Phys. Fluids **21**, 022104 (2009).
[16] T. J. Asaki and P. L. Marston, J. Fluid Mech. **300**, 149 (1995).
[17] R. G. Holt and D. F. Gaitan, Phys. Rev. Lett. **77**, 3791 (1996).
[18] M. P. Brenner, D. Lohse, and T. F. Dupont, Phys. Rev. Lett. **75**, 954 (1995).
[19] S. Hilgenfeldt, D. Lohse, and M. P. Brenner, Phys. Fluids **8**, 2808 (1996).
[20] Y. Tian, J. A. Ketterling, and R. E. Apfel, J. Acoust. Soc. Am. **100**, 3976 (1996).
[21] E. H. Trinh, D. B. Thiessen, and R. G. Holt, J. Fluid Mech. **364**, 253 (1998).
[22] Y. Hao and A. Prosperetti, Phys. Fluids **11**, 1309 (1999).
[23] M. Kameda and Y. Matsumoto, J. Acoust. Soc. Am. **106**, 3156 (1999).
[24] M. P. Brenner, S. Hilgenfeldt, and D. Lohse, Rev. Mod. Phys. **74**, 425 (2002).
[25] D. F. Gaitan and R. G. Holt, Phys. Rev. E **59**, 5495 (1999).
[26] T. J. Matula, Philos. Trans. R. Soc. London, Ser. A **357**, 225 (1999).
[27] P. Palanchon, J. Klein, and N. de Jong, Rev. Sci. Instrum. **74**, 2558 (2003).
[28] See supplementary material at http://link.aps.org/supplemental/10.1103/PhysRevE.82.026321. Ultra high-speed recording of an oscillating air bubble developing a surface mode vibration, here with mode number $n=4$, through a parametric instability. The 36 micrometer radius bubble is driven by a 10–cycle ultrasound pulse at a frequency of 130 kHz at a acoustic pressure of 120 kPa. The movie is captured at a frame rate of 1.25 million frames per second.
[29] C. T. Chin *et al.*, Rev. Sci. Instrum. **74**, 5026 (2003).
[30] M. Sonka, V. Hlavac, and R. Boyle, *Image Processing, Analysis, and Machine Vision* (Thompson Learning, Toronto, 2008).
[31] P. Morse and H. Feshbach, *Methods of Theoretical Physics* (McGraw Hill, New York, 1953).
[32] H. Lamb, *Hydrodynamics* (Cambridge University Press, Cambridge, England, 1932).
[33] A. Francescutto and R. Nabergoj, Acustica **41**, 215 (1978).
[34] J. B. Keller and M. J. Miksis, J. Acoust. Soc. Am. **68**, 628 (1980).
[35] C. Devin, J. Acoust. Soc. Am. **31**, 1654 (1959).
[36] H. Medwin, Ultrasonics **15**, 7 (1977).
[37] R. Toegel and D. Lohse, J. Chem. Phys. **118**, 1863 (2003).
[38] R. Toegel, S. Hilgenfeldt, and D. Lohse, Phys. Rev. Lett. **88**, 034301 (2002).
[39] M. P. Brenner, T. F. Dupont, S. Hilgenfeldt, and D. Lohse, Phys. Rev. Lett. **80**, 3668 (1998).
[40] C. E. Brennen, J. Fluid Mech. **472**, 153 (2002).
[41] B. Dollet *et al.*, Ultrasound Med. Biol. **34**, 1465 (2008).